RSC Advances

PAPER

View Article Online
View Journal | View Issue

Cite this: *RSC Adv.*, 2023, **13**, 18122

Massively synthesizable nickel-doped 1T-MoS_2 nanosheet catalyst as an efficient tri-functional catalyst†

Yusong Choi, *[ab] Tae-Young Ahn, [a] Ji-Youn Kim,[ac] Eun Hye Lee[a] and Hye-Ryeon Yu[ad]

Received 6th May 2023
Accepted 9th June 2023

DOI: 10.1039/d3ra03016d

rsc.li/rsc-advances

In this study, a nickel (Ni)-doped 1T-MoS_2 catalyst, an efficient tri-functional hydrogen evolution reaction (HER), oxygen evolution reaction (OER), and oxygen reduction reaction (ORR) catalyst, was massively synthesized at high pressure (over 15 bar). The morphology, crystal structure, and chemical and optical properties of the Ni-doped 1T-MoS_2 nanosheet catalyst were characterized by transmission electron microscopy (TEM), X-ray diffraction (XRD), X-ray photoelectron spectroscopy (XPS), and ring rotating disk electrodes (RRDE), and the OER/ORR properties were characterized using lithium-air cells. Our results confirmed that highly pure, uniform, monolayer Ni-doped 1T-MoS_2 can be successfully prepared. The as-prepared catalysts exhibited excellent electrocatalytic activity for OER, HER, and ORR owing to the enhanced basal plane activity of Ni doping and formidable active edge sites resulting from the phase transition to a highly crystalline 1T structure from 2H and amorphous MoS_2. Therefore, our study provides a massive and straightforward strategy to produce tri-functional catalysts.

Introduction

In recent years, there have been intensive efforts to explore nanostructured catalysts based on transition metals and their alloys, such as sulphides,[1–3] selenides, carbides, nitrides, and phosphides, as potential noble-metal-free electrocatalysts. Layered transition metal dichalcogenides (TMDs), such as molybdenum disulphide (MoS_2) and tungsten disulphide (WS_2), have been investigated as energy materials, catalysts for hydrogen energy synthesis, and gas sensing materials over the past decades due to their unique chemical, economic, and abundant properties.[4] In particular, MoS_2 has gained increasing attention owing to its high electronic conductivity, mechanism, and high theoretical capacity,[5–7] making it one of the most promising electrode materials for supercapacitors, photocatalytic, and Li-ion batteries.[8–10]

Moreover, MoS_2 has been studied as a promising hydrogen evolution reaction (HER) catalyst meeting both technical and economic requirements[11–13]. As the world is moving towards using carbon-free energy sources, called the 'hydrogen economy', the demand for efficient and non-precious HER catalysts has increased.[14,15] Many attempts have been made to clarify the catalytic mechanism with various crystallographic structures and morphologies of MoS_2, including chemically exfoliated MoS_2,[16,17] nanostructured particles,[18–21] heterostructures, and amorphous and doped MoS_2. To date, experimental and computational studies have reported that the edge sites of crystalline MoS_2 are catalytically active, whereas their basal planes are inert. Therefore, the best approaches for improving the catalytic functionality of MoS_2 are to generate an active edge site, incorporate doping elements, or convert crystal structures.

For instance, the metallic 1T-MoS_2 octahedral symmetry improves the HER performance of MoS_2, as it has great potential for activating basal planes in contrast to the traditional trigonal prismatic semi-conducting 2H-phase MoS_2 (see the crystal structure of 2H and 1T shown in Fig. S1†). Many reports have indicated the high performance of metallic 1T-MoS_2, especially when the basal planes are tethered with a single-atom catalyst. Single-atom tethering or doping of the MoS_2 basal plane can effectively enhance the catalytic activity of 1T-MoS_2.

Recently, NiMoS (Ni–MoS_2) heterostructure electrodes have been studied as water-splitting electrodes due to their excellent HER[22] and oxygen evolution reaction (OER) activities.[10–12] In addition, Ni-doped MoS_2 nanorods[23] and nanoflakes synthesized in Ni-doped forms have been reported. However, there are no reports on the use of massively synthesizable tri-functional Ni-doped 1T-MoS_2 as electrocatalysts. Therefore, in this study,

[a]*Defense Materials and Energy Development Center, Agency for Defense Development, Yuseong P.O. Box 35, Daejeon, 34060, Korea. E-mail: richpine87@gmail.com*

[b]*Department of Defense System Engineering, University of Science and Technology, Daejeon 34113, Korea*

[c]*Department of Chemical and Biomolecular Engineering, KAIST, 291 Daehak-ro, Yuseong-gu, Daejeon 34141, Republic of Korea*

[d]*Department of Chemical Engineering and Applied Chemistry, Chungnam National University, Daejeon 34134, Korea*

† Electronic supplementary information (ESI) available. See DOI: https://doi.org/10.1039/d3ra03016d

to utilize the excellent electrocatalytic properties of Ni-doped MoS_2 for next-generation energy synthesis, Ni-doped MoS_2 was fabricated using Ni particles, and their electrocatalytic properties were investigated.

Experimental methods

Ni-doped MoS_2 synthesis

The synthesis of Ni-doped MoS_2 using nickel particles (particle size: 10 μm, 99.9%, Sigma-Aldrich) followed a previously reported method.[24] Prior to synthesis, 200 g of Ni particles were sequentially prepared and sonicated in water, 0.1 M HCl, and acetone for 30 min. Subsequently, the dried nickel particles were immersed in 800 mL of *N*,*N*-dimethylformamide (DMF, anhydrous, 99.8%, Sigma-Aldrich) solution containing 320 mg of ammonium tetrathiomolybdate ($(NH_4)_2MoS_4$, 99.97%, Sigma-Aldrich), as shown in Fig. 1. They were heated at 200 °C in a Teflon autoclave (1000 mL) for 12 h during hydrothermal synthesis with a stirring at an rpm of 200. The pressure was maintained above 15 bar. After rinsing with water and ethanol, more than 200 g of homogeneous Ni-doped MoS_2 powder was obtained. As-received MoS_2 (99.97%, Sigma-Aldrich) was also prepared for comparison.

Microstructural observation

After the hydrothermal synthesis of the samples, their chemical compositions and microstructures were characterized using scanning electron microscopy (SEM; FEI-QUANTA650) and transmission electron microscopy (TEM; Jeol, JEM-ARM200F) equipped with energy dispersive spectroscopy (EDS) and electron energy loss spectroscopy (EELS).

X-ray photoelectron spectroscopy (XPS) analysis

The surface chemistries of the synthesized MoS_2 samples were analysed using XPS (Thermo Fischer Scientific K-Alpha+ XPS; the X-ray source was Kα 200 mm). The surface was argon etched before the XPS analysis.

Electrocatalytic properties

HER experiments were performed with a three-electrode measurement method. Platinum was used as the counter electrode, and Ag/AgCl as the reference electrode. The working electrode samples prepared on the working electrode are made of glassy carbon. A 10 mg sample was dispersed using a bath sonicator in 1 mL water–ethanol (1 : 1 v/v) solution containing 25 μL Nafion solution (5 wt%), with 10 μL of the dispersed solution drop cast on the working electrode and dried before electrochemical testing. All electrochemical analyses were carried out in an N_2-saturated 0.5 M H_2SO_4 electrolyte at 25 °C. Electrochemical impedance spectroscopy (EIS) studies were performed in the frequency range of 5 mHz to 10 kHz, with an AC amplitude of 10 mV applied to all measurements.

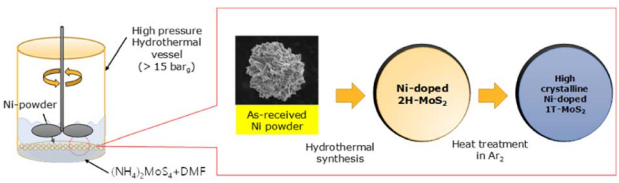

Fig. 1 Schematic of synthesis of Ni-doped 1T MoS_2 tri-functional catalysts.

Full cell fabrication and electrochemical measurements

The Ni-doped MoS_2 was filtered with CNT solution (multi-walled CNT 0.18 g; cm-250 Hanwha Chemical, South Korea) in 1 L of distilled water–isopropyl alcohol (IPA, 99.999% Sigma-Aldrich, South Korea) in a ratio of 4 : 1, sonicated with a pulse (on and off for 3 and 1 s, respectively) for 10 min, and filtered. The filtered sample was dried in a dry oven at 90 °C overnight. The filtered cathode was peeled off from the filter and then punched to 12 mm in diameter for coin cell fabrication (the sample loading was 1 mg cm^{-2}). Celgard® 2400 (Celgard, USA) material was used as a separator. The electrolyte was 1.0 M bis(trifluoromethane) sulfonamide lithium (LiTFSI) in triethylene glycol dimethyl ether (TEGDME) (Sigma-Aldrich, South Korea). For comparison, IrO_2 (99.9% purity, Aldrich) and Pt/C (Pt 20% on carbon black, Alfa aesar) were also fabricated with the same filtration method. To study the full-cell performance, pure lithium as an anode and CNT (with and without Ni-doped MoS_2) cathode were fabricated using a CR 2032 coin cell. The cathode side of the coin cell was opened with 1 mm diameter holes. After assembling symmetric cells, all cells were cycled at a 0.005 mA h cm^{-1} (charge and discharge current density were 0.005 mA cm^{-2}) to the cut-off voltage of 2 V.

Results and discussion

TEM images of synthesized MoS_2 are shown in Fig. S2.† As the synthesized Ni-doped MoS_2 is an amorphous sheet, several crystal nanoparticles similar to the quantum dots exist on it, as shown in Fig. S2(a) and (b).† After heat-treatment at 500 °C, the amorphous 2D MoS_2 sheet was converted to the crystal structure, as shown in Fig. S2(c).† It is worth mentioning that there are many reports on microsized crystal MoS_2 structure on an amorphous 2D MoS_2 sheet but crystal structure change investigation nano-sized Ni-doped MoS_2 on 2D amorphous MoS_2 sheet after heat-treatment. Fig. 2 shows the high-resolution transmission electron micrographs (HRTEM) of the prepared Ni-doped MoS_2. The HRTEM image in Fig. 2(a) shows a single Ni-doped MoS_2 nanoparticle after hydrothermal synthesis. The measured interplanar distance of 0.253 nm corresponded to the typical spacing of the lattice of MoS_2 (110) at 0.253 nm. The mean size of prepared Ni-doped MoS_2 was approximately 10 nm. In addition to the Ni-doped MoS_2 nanocrystals, most 2D sheets show an amorphous phase, as shown in Fig. S2.† The electron energy loss spectroscopy (EELS) is shown in Fig. 2(c). The Ni L edge line Ni spectra between 808.8 and 831.9 eV of the synthesized Ni-doped MoS_2 are ascribed to the doped Ni in MoS_2.

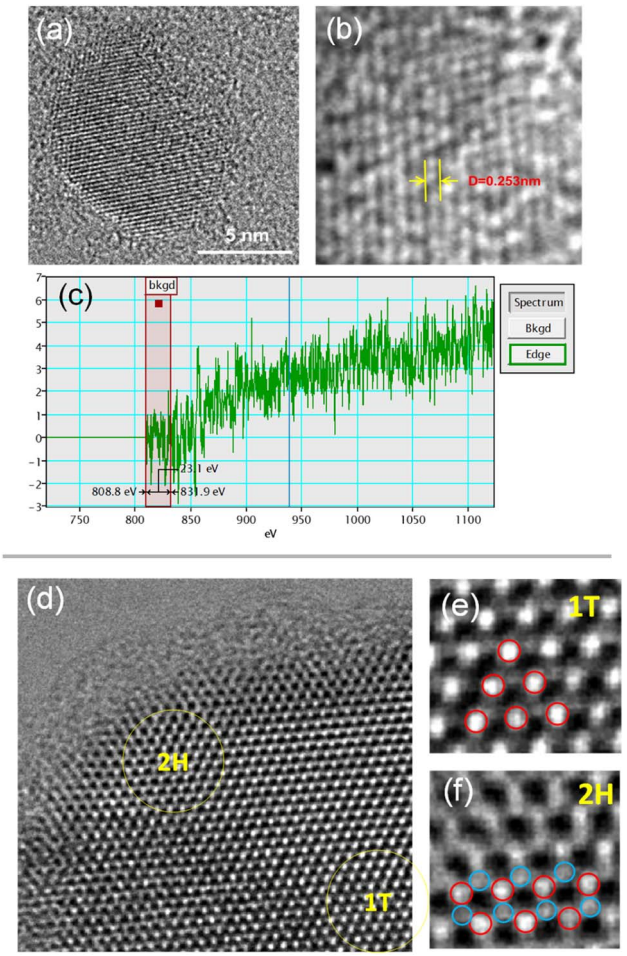

Fig. 2 (a) TEM image of Ni-doped MoS_2 nanoparticles, (b) *d*-spacing of Ni-doped-MoS_2 nanoparticles, (c) electron energy loss spectroscopy (EELS) spectra of Ni L edge line, (d) HRTEM image of Ni-doped-MoS_2, (e) 1T Ni-doped-MoS_2 on centre (blue circle is molybdenum), (f) 2H Ni-doped MoS_2 on edge (red circle is molybdenum and the blue circle is sulphur).

The HRTEM image of Ni-doped MoS_2 after heat treatment is shown in Fig. 2(d). The edge of the Ni-doped MoS_2 nanoparticle shows a 2H phase, while the centre shows a 1T phase, as shown in Fig. 2(e) and (f).

The crystal structure of the Ni-doped 1T-MoS_2 was investigated (Fig. S3†), and the peaks at 21.8°, 31.4°, 38.3°, 49.7°, and 50.1° are assigned to the (101), (101), (003), (113), and (211) planes of MoS_2 (JCPDS 44-1418).[25,26] Conversely, the peaks at 44.5°, 51.8°, and 76.4° were consistent with those of Ni (JCPDS 11-0099). In the X-ray diffraction (XRD) peaks of Ni-doped 1T-MoS_2, in contrast to pure MoS_2, the diffraction peaks of Ni-doped MoS_2 shifted slightly above 44.63°. These shifts indicate that the lattice parameters of doped MoS_2 increase because of the larger ion size of Mo than that of Ni. This 1T Ni-doped MoS_2 structure changes after heat-treatment of Ni-doped MoS_2, as shown in Fig. S4.†

An XPS analysis was performed to investigate the chemical valence states of these elements (the full XPS spectrum has been provided in Fig. S4†). The XPS spectrum of the MoS_2 series in the Mo 3d region can be divided into four peaks (Fig. 3(a)). The peak at 225 eV corresponds to S 2s of the MoS_2 series.[27] The minor peak (236.0 eV) is attributed to Mo^{6+}, which corresponds to the slight oxidation of the Mo edges of MoS_2 upon exfoliation, as reported by Gopalakrishnan *et al.*[28] The Mo 3d peaks of the received MoS_2 and Ni-doped MoS_2 as a function of heat treatment, were observed as shown in Fig. 3(a) and (b), respectively. The two intense peaks at approximately 231 and 228 eV being ascribed to Mo $3d_{3/2}$ and Mo $3d_{5/2}$, respectively, should be attributed to the Mo^{4+} in the MoS_2 series.[29–31] As observed in Fig. 3(a), the MoS_2 showed a 2H-phase based on the Mo $3d_{5/2}$ and Mo $3d_{3/2}$ orbitals with peaks at 228.6–228.7 eV and 231.8–231.9 eV, respectively.

However, a noticeable red shift of Mo $3d_{5/2}$ and Mo $3d_{3/2}$ orbitals was observed for the Ni-doped MoS_2, according to the heat-treatment condition (in Fig. 3(b)), which is believed to represent the 2H to 1T phase shift of MoS_2.[32,33] It has been reported that, when the phase transition from 2H to 1T occurs, the $3d_{5/2}$ and $3d_{2/3}$ components of Mo–S bonding in XPS is measured to be about 1 eV lower.[34,35] Therefore, this result is consistent with the decrease in binding energy (~1.1 eV) of Mo $3d_{3/2}$ upon heat-treatment. The Raman analysis results demonstrate the 1T in the 2H MoS_2 structure occurrence after heat-treatment (Fig. S5†).

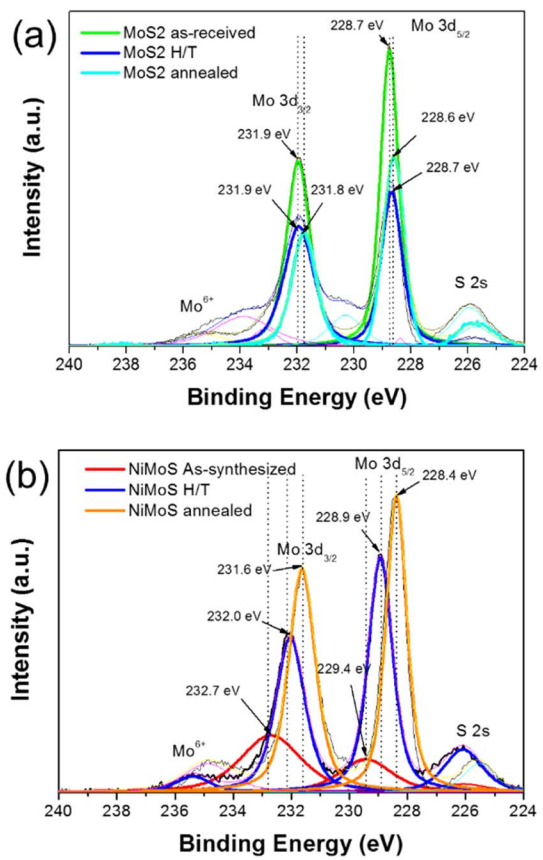

Fig. 3 The XPS spectra of Mo 3d for (a)MoS_2 and (b) Ni-doped MoS_2 series as-synthesized after heat treatment and annealing.

Based on XPS and XRD results, it can be concluded that the crystal structure transformation of Ni-doped MoS_2 from the 2H to 1T phase occurred during heat treatment. EDS element mapping analysis showed a uniform distribution of Ni, Mo, and S throughout the entire grid of Ni-doped 1T-MoS_2 specimens (see Fig. S6†).

Fig. 4(a) shows HER Tafel plots of Ni-doped MoS_2. Pt/C was also studied for comparison. Fig. S7† shows the RHE calibration. The potential was swept at 1 mV s^{-1} in H_2-saturated 1 M KOH. Pt wires were used as working and counter electrodes, while Ag/AgCl was used as a reference electrode. For detailed electrochemical analysis, RHE calibration was conducted with Pt wires and Ag/AgCl (saturated KCl) reference electrodeFig. S7.† The RHE calibration was calculated using the following eqn (1),

$$E_{RHE} = E_{measured\ by\ Ag/AgCl} + 1.029\ V \quad (1)$$

Among all the catalysts tested, both as-synthesized and heat-treated Ni-doped MoS_2 exhibited inferior catalytic activities for the HER with overpotentials. However, the stability of the heat-treated Ni-doped MoS_2 was much higher than that of Pt/C over 2500 s. The semicircle of the heat-treated Ni-doped MoS_2 in the Nyquist plot shown in Fig. 4(c) decreased significantly following heat treatment. The decrease in resistance is ascribed to the increase in crystallinity and the phase transition from 2H to the metallic 1T structure of MoS_2.

Pattenggale *et al.*[36] and Huang *et al.*[37] reported Ni@1T-MoS_2 for HER. Pattengale reported remarkable HER performance compared to Pt/C in both acidic and alkaline solutions. Pattengale *et al.* reported that the remarkable HER performance is attributed to the Ni sites in the basal plane of Ni@1T-MoS_2, which are active towards HER. Pattengale *et al.* and Huang *et al.* synthesized Ni@1T-MoS_2 by hydrothermal synthesis; however, they reported two steps. First, the $NiMo_6$ precursor was synthesized, and then sulfuration to $NiMo_6$ was carried out.

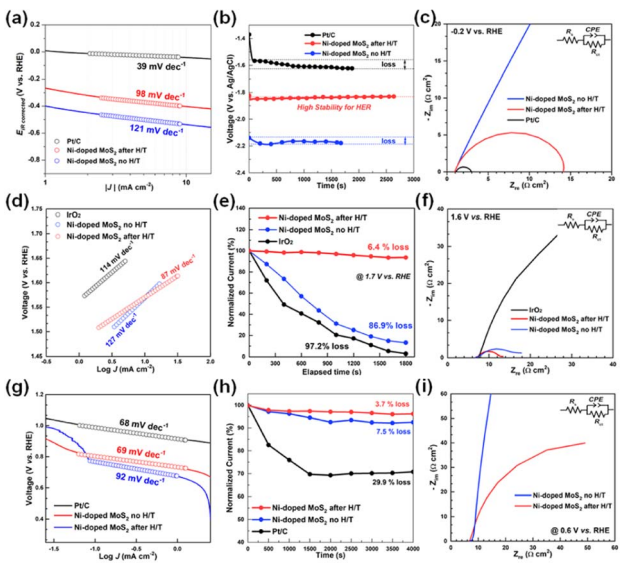

Fig. 4 RRDE analysis results in (a) HER Tafel plot for Pt/C, as-synthesized Ni-doped MoS_2, and heat-treated MoS_2, (b) HER stabilities, (c) Nyquist plot during the HER performance analysis, (d) OER Tafel plot for Pt/C, as-synthesized Ni-doped MoS_2, and heat-treated MoS_2, (e) OER stabilities, (f) Nyquist plot during the OER performance analysis, (g) ORR Tafel plot for Pt/C, as-synthesized Ni-doped MoS_2, and heat-treated MoS_2, (h) ORR stabilities, (i) Nyquist plot during the ORR performance analysis.

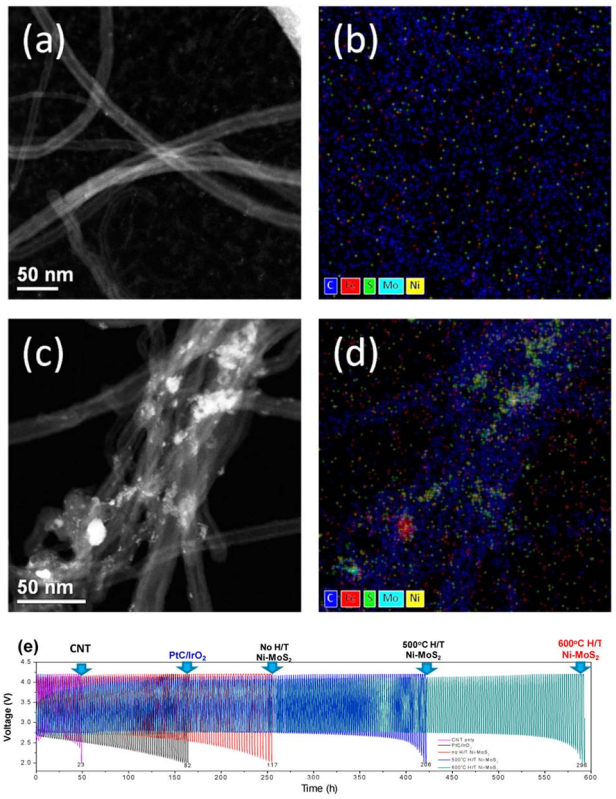

Fig. 5 (a) Dark-field TEM image of the control CNT electrode, (b) TEM EDS mapping image of the control CNT electrode, (c) dark field TEM image of the Ni-doped MoS_2 CNT electrode, (d) TEM EDS mapping image of the Ni-doped MoS_2 CNT electrode (e) cycle performance comparison for the CNT, Pt/C/IrO_2, as-synthesized (no heat treatment) Ni-doped MoS_2, 500 °C heat treated Ni–MoS_2 and 600 °C heat treated Ni-doped MoS_2.

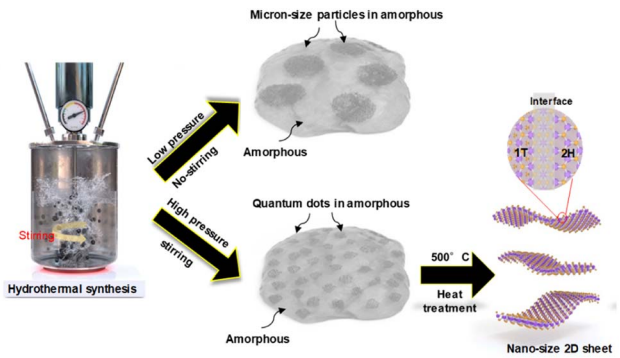

Fig. 6 The schematic of the proposed Ni-doped MoS_2 morphology and crystal structure varies according to the hydrothermal synthesis conditions (applying the stirring and pressure control).

OER properties were also studied, as shown in Fig. 4(d)–(f). For Ni-doped MoS_2 after heat-treatment, a lower Tafel slope of 87 mV dec^{-1} is observed. In contrast, higher Tafel slopes of 114 and 127 mV dec^{-1} were obtained for IrO_2 and as-synthesized Ni-doped MoS_2, respectively. Ni-doped MoS_2 exhibited ORR activity with a low overpotential of 68 mV. It is worth noting that Ni-doped MoS_2 series show superior activity to those of the reported MoS_2, Ni-doped MoS_2 nanorods, nanosheets, and most of the reported non-noble metal-based ORR catalysts. The corresponding Tafel plots were used to estimate the ORR kinetics of these electrodes (Fig. 4(g)).

To evaluate the OER/ORR stability of Ni-doped MoS_2 in 1 M KOH solution, we measured the time-dependent potential curve at 10 mA cm^{-2}. As shown in Fig. 4(e) and (h), even after the 2700 s continuous release of oxygen, the potential of network Ni-doped MoS_2 after heat-treatment is still well maintained, implying excellent long-term durability for the OER and ORR. The semicircles of heat-treated Ni-doped MoS_2 in the Nyquist plot shown in Fig. 4(f) and (i) decreased significantly following the heat treatment. The decrease in resistance accounts for the increase in crystallinity and the phase transition from 2H to the metallic 1T structure of MoS_2. The results suggest that the prepared Ni-doped MoS_2 series catalyst exhibited strong catalytic activity and stability during the OER and ORR processes. The specific surface area (SSA) plays a vital role in electrochemical activities. To better understand the intrinsic properties of each catalyst, their SSA was estimated using the Brunauer–Emmett–Teller (BET) technique, as shown in Fig. S8.† The Ni-doped MoS_2 after the H/T catalyst shows much higher specific activity than the Ni-doped MoS_2 no H/T catalyst for HER, ORR, and OER. Interestingly, the specific current density of the Ni-doped MoS_2 after the H/T catalyst is much higher than the state-of-art Pt/C and IrO_2 for the ORR and OER process. Overall, the Ni-doped MoS_2 after the H/T catalyst is an excellent electrocatalyst with great promise for practical application.

Furthermore, it affords only a 0.835 V polarization gap between OER and ORR for Ni-doped MoS_2 after heat treatment, making it among the most active reported electrocatalysts. For comparison, Pt/C and IrO_2 were also measured, and the total polarization of Pt/C IrO_2 was 0.837 V (see Fig. S9†).

The OER and ORR performance of Ni-doped MoS_2 according to the heat-treatment effect was studied using full cells. For comparison, a Pt/C/IrO_2 cell was also fabricated, as shown in Fig. 5. After the filtration and drying, the cathode was examined using TEM. Fig. 5(a)–(d) shows the TEM analysis results. Fig. 5(a) and (b) show the CNT-only sample of dark field TEM image and TEM EDS mapping image, respectively. As shown in Fig. 5(a) and (b), only CNT and carbon from CNT exist. However, in Fig. 5(c) and (d), the Ni-doped MoS_2 catalysts adhere well to the CNT fibres. These samples were fabricated to the full cell (CR 2032) to investigate the real OER and ORR performance. For comparison, IrO_2 and Pt/C were also fabricated with the filtration method.

All cells were cycled at a 0.05 mA h cm^{-1} cut-off voltage of 2 V, and the results are shown in Fig. 5(e). The Ni-doped MoS_2 cells exhibited better cycle performance than Pt/C/IrO_2 cells. The Pt/C/IrO_2 cell cycled for 160 h, and synthesized Ni-doped MoS_2 cycled for 247 h, which is a 55% increase. However, above 500 and 600 °C, the heat-treatment times to reach the cut-off (2 V) were 400 and 560 h, respectively. The cycle performance improved significantly with increased heat-treatment temperature and time.

After the cycle test, the cathodes were disassembled, and XRD analysis was conducted, as shown in Fig. S10.† There is no carbon electrode decomposition evidence of Li_2CO_3 by the reaction with oxygen as well as carbon has not been found. The drastically enhanced OER and ORR performance of Ni-doped MoS_2 over Pt/C/IrO_2 can be ascribed to the increase in crystallinity and the phase shift from 2H to 1T-MoS_2 following heat treatment. The results indicate that the proposed massively synthesizable Ni-doped 1T-MoS_2 tri-functional catalyst has robustness, good cyclability, and applicability as a next-generation lithium–air battery electrode.

Based on the structural and catalytic analysis results for the hydrothermally synthesized Ni-doped MoS_2, we investigated the proposed structure tailoring path, as shown in Fig. 6. Ni-doped MoS_2 microsized particles in 2D amorphous MoS_2 were synthesized through conventional hydrothermal synthesis (no stirring and low pressure at 4–5 bar). However, Ni-doped MoS_2 nanoparticles in 2D amorphous MoS_2 synthesized at high pressure (over 15 bar) with stirring were applied during hydrothermal synthesis. Heat treatment at 500 °C was conducted on the Ni-doped MoS_2 nanoparticles in 2D amorphous MoS_2, synthesized at high pressure and converted to a highly crystalline 2D nanosheet with a 1T structure, which showed stable and efficient tri-functional catalytic performance for HER, OER, and ORR.

Conclusions

Ni-doped MoS_2 was successfully synthesized *via* a hydrothermal process. Ni-doped MoS_2 exhibits superior performance and stability as a tri-functional electrocatalyst for HER, OER, and ORR as a highly active electrode. Furthermore, it affords only a 0.835 V polarization gap between OER and ORR for Ni-doped MoS_2 after heat treatment, making it among the most active reported electrocatalysts. For comparison, Pt/C and IrO_2 were also measured, and the total polarization of Pt/C IrO_2 was 0.837 V. This high catalytic activity can be attributed to the 1T MoS_2 structure resulting from Ni doping. Specifically, the increased surface area of the series with high exposure to active sites could greatly facilitate mass/charge transfer, close contact with the electrolyte, and facile release of the evolved gas during ORR and OER catalysis. Moreover, the *in situ* grown Ni-doped MoS_2 may further increase the conductivity and charge transfer capability. This work suggests promising, novel, and highly efficient ternary transitions for electrocatalysts.

Author contributions

Yusong Choi: conceptualization, writing – original draft and editing, fund acquisition, supervision, Tae-Young Ahn: methodology, investigation, writing – original draft, data curation,

result discussion, Ji-Youn Kim: methodology, investigation, data curation, Eun Hye Lee: methodology, investigation, data curation, Hye-Ryeon Yu: methodology, investigation, writing – original draft and editing.

Conflicts of interest

There are no conflicts to declare.

Acknowledgements

This work was supported by the Defense Acquisition Program Administration by the Korean Government (911132202).

References

1 S. Deng, Y. Zhong, Y. Zeng, Y. Wang, X. Wang, X. Lu, X. Xia and J. Tu, *Adv. Sci.*, 2018, **5**, 1700772.
2 Y. Yang, K. Zhang, H. Lin, X. Li, H. c. Chan, L. Yang and Q. Gao, *ACS Catal.*, 2017, **7**, 2357–2366.
3 X. Zhu, T. Jin, C. Tian, C. Lum, X. Liu, M. Zeng, X. Zhuang, S. Yang, L. He, H. Liu and S. Dai, *Adv. Mater.*, 2017, **29**, 2357–2366.
4 B. N. Pal, Y. Ghosh, S. Brovelli, R. Laocharoensuk, V. I. Klimov, J. A. Hollingsworth and H. Htoon, *Nano Lett.*, 2011, **12**, 331–336.
5 H. J. Kim, D. J. Kim, S. Srinivasa Rao, A. Dennyson Savariraj, K. Soo-Kyoung, M. K. Son, C. V. V. M. Gopi and K. Prabakar, *Electrochim. Acta*, 2014, **127**, 427–432.
6 H. J. Kim, S. W. Kim, C. V. V. M Gopi, S. K. Kim, S. S. Rao and M. S. Jeong, *J. Power Sources*, 2014, **268**, 163–170.
7 S. C. Han, K. W. Kim, H. J. Ahn and J. Y. Lee, *J. Alloys Compd.*, 2003, **361**, 247–251.
8 T. Zhu, H. B. Wu, Y. Wang, R. Xu and X. W. Lou, *Adv. Eng. Mater.*, 2012, **2**, 1497–1502.
9 J. J. Wang, Z. J. Li, X. B. Li, X. B. Fan, Q. Y. Meng, S. Yu, C. B. Li, J. X. Li, C. H. Tung and L. Z. Wu, *ChemSusChem*, 2014, **7**, 1468–1475.
10 J. Z. Wang, S. L. Chou, S. Y. Chew, J. Z. Sun, M. Forsyth, D. R. MacFarlane and H. K. Liu, *Solid State Ionics*, 2008, **179**, 2379–2382.
11 T. F. Jaramillo, K. P. Jørgensen, J. Bonde, J. H. Nielsen, S. Horche and I. Chorkendorff, *Science*, 2007, **317**(5834), 100–102.
12 A. B. Laursen, S. Kegnæs, S. Dahl and I. Chorkendorff, *Energy Environ. Sci.*, 2012, **5**(2), 5577–5591.
13 G. Q. Li, D. Zhang, Q. Qiao, Y. F. Yu, D. Peterson, A. Zafar, R. Kumar, S. Curtarolo, F. Hunte, S. Shannon, Y. Zhu, W. T. Yang and L. Y. Cao, *J. Am. Chem. Soc.*, 2016, **138**(51), 16632–16638.
14 J. A. Turner, *Science*, 2004, **305**(5686), 972–974.
15 M. S. Dresselhaus and I. L. Thomas, *Nature*, 2001, **414**(6861), 332–337.
16 D. Voiry, M. Salehi, R. Silva, T. Fujita, M. Chen, T. Asefa, V. B. Shenoy, G. Eda and M. Chhowalla, *Nano Lett.*, 2013, **13**(12), 6222–6227.
17 M. A. Lukowski, A. S. Daniel, F. Meng, A. Forticaux, L. Li and S. Jin, *J. Am. Chem. Soc.*, 2013, **135**(28), 10274–10277.
18 J. Yang and H. S. Shin, *J. Mater. Chem. A*, 2014, **2**(17), 5979–5985.
19 B. Hinnemann, P. G. Moses, J. Bonde, K. P. Jørgensen, J. H. Nielsen, S. Horch, I. Chorkendorff and J. K. Nørskov, *J. Am. Chem. Soc.*, 2005, **127**(15), 5308–5309.
20 M. L. Tang, D. C. Grauer, B. Lassalle-Kaiser, V. K. Yachandra, L. Amirav, J. R. Long, J. Yano and A. P. Alivisatos, *Angew. Chem., Int. Ed. Engl.*, 2011, **50**(43), 10203–10207.
21 Y. G. Li, H. Wang, L. Xie, Y. Liang, G. Hong and H. Dai, *J. Am. Chem. Soc.*, 2011, **133**(19), 7296–7299.
22 Y. Hao, Y. T. Wang, L. C. Xu, Z. Yang, R. P. Liu and X. Y. Li, *Appl. Surf. Sci.*, 2019, **469**, 292–297.
23 Z. Cui, Y. Ge, H. Chu, R. Baines, P. Dong, J. Tang, Y. Yang, P. M. Ajavan, M. Ye and J. Shen, *J. Mater. Chem. A*, 2017, **5**, 1595–1602.
24 Y. S. Choi, T.-Y. Ahn, S.-H. Ha and J.-H. Cho, *Chem. Commun.*, 2019, **55**, 7300.
25 N. Jiang, Q. Tang, M. Sheng, B. You, D. E. Jiang and Y. Sun, *Catal. Sci. Technol.*, 2016, **6**, 1077–1084.
26 T. W. Lin, C. J. Liu and C. S. Dai, *Appl. Catal., B*, 2014, **154**, 213–220.
27 X. Ren, L. Pang, Y. Zhang, X. Ren, H. Fan and S. Liu, *J. Mater. Chem. A*, 2015, **3**, 10693.
28 D. Gopalakrishnan, D. Damien and M. M. Shaijumon, *ACS Nano*, 2014, **8**, 5297–5303.
29 B. L. Li, L. X. Chen, H. L. Zou, J. L. Lei, H. Q. Luo and N. B. Li, *Nanoscale*, 2014, **6**, 9831–9838.
30 H. Lin, C. Wang, J. Wu, Z. Xu, Y. Huang and C. Zhang, *New J. Chem.*, 2015, **39**, 8492–8497.
31 Y. Wang, S. Wang, C. Li, M. Qian, J. Bu, J. Wang and R. Huang, *Chem. Commun.*, 2016, **52**, 10217–10220.
32 X. Wang, Q. Wu, K. Jiang, C. Wang and C. Zhang, *Sens. Actuators, B*, 2017, **252**, 183–190.
33 Y. C. Lin, D. O. Dumcenco, D. Y. S. Huang and K. Suenaga, *Nat. Nanotechnol.*, 2014, **9**, 391.
34 X. Geng, Y. Jiao, Y. Han, A. Mukhopadhyay, L. Yang and H. Zhu, *Adv. Funct. Mater.*, 2017, **27**, 1702998.
35 X. Geng, W. Sun, W. Wu, B. Chen, A. Al-Hilo, M. Benamara, H. Zhu, F. Watanabe, J. Cui and T. P. Chen, *Nat. Commun.*, 2016, **7**, 10672.
36 B. Pattengale, Y. Huang, X. Yan, S. Yang, S. Younan, W. Hu, Z. Li, S. Lee, X. Pan, J. Gu and J. Huang, *Nat. Commun.*, 2020, **11**, 4114.
37 Y. Huang, Y. Sun, X. Zheng, T. Aoki, B. Pattengale, J. Huang, X. He, W. Bian, S. Younan, N. Williams, J. Hu, J. Ge, N. Pu, X. Yan, X. Pan, L. Zhang, Y. Wei and J. Gu, *Nat. Commun.*, 2019, **10**, 1–11.